

Nanoscale Bubble Domains and Topological Transitions in Ultrathin Ferroelectric Films

Qi Zhang, Lin Xie, Guangqing Liu, Sergei Prokhorenko, Yousra Nahas, Xiaoqing Pan, Laurent Bellaiche, Alexei Gruverman, and Nagarajan Valanoor*

Observation of a new type of nanoscale ferroelectric domains, termed as “bubble domains”—laterally confined spheroids of sub-10 nm size with local dipoles self-aligned in a direction opposite to the macroscopic polarization of a surrounding ferroelectric matrix—is reported. The bubble domains appear in ultrathin epitaxial $\text{PbZr}_{0.2}\text{Ti}_{0.8}\text{O}_3/\text{SrTiO}_3/\text{PbZr}_{0.2}\text{Ti}_{0.8}\text{O}_3$ ferroelectric sandwich structures due to the interplay between charge and lattice degrees of freedom. The existence of the bubble domains is revealed by high-resolution piezoresponse force microscopy (PFM), and is corroborated by aberration-corrected atomic-resolution scanning transmission electron microscopy mapping of the polarization displacements. An incommensurate phase and symmetry breaking is found within these domains resulting in local polarization rotation and hence impart a mixed Néel–Bloch-like character to the bubble domain walls. PFM hysteresis loops for the bubble domains reveal that they undergo an irreversible phase transition to cylindrical domains under the electric field, accompanied by a transient rise in the electromechanical response. The observations are in agreement with ab-initio-based calculations, which reveal a very narrow window of electrical and elastic parameters that allow the existence of bubble domains. The findings highlight the richness of polar topologies possible in ultrathin ferroelectric structures and bring forward the prospect of emergent functionalities due to topological transitions.

domains,^[3,4] Néel-like domain walls^[5,6] incommensurate curl domains,^[7] and ferrotoroidic domains^[8] have been experimentally reported. The technological interest in these structures is driven by their emergent physical properties, such as nanomagnetism in multiferroic vortices,^[9] dynamic conduction,^[10] and chirality^[11] which may be exploited for ultrahigh (exceeding tens of Tb in⁻²) memory densities, low power consumption, and colossal electromechanical activity.^[12,13]

One class of topological defects that is both fundamentally and technologically exciting is nanoscale spheroid ferroelectric bubble domains.^[14] Theoretical predictions stipulate that for such domains to be stable, they must have both in-plane and out-of-plane polarization components,^[14,15] and the interface between the bubble and the ferroelectric matrix must show polarization rotation to minimize the dipole flux,^[16] resulting in large polarization gradients. This is a key feature that distinguishes bubble domains from regular cylindrical domains with uniform distribution of polarization. Second, just as modern chiral skyrmions^[17,18] can be topologically identical to classical magnetic bubble domains,^[19] ferroelectric bubble domains can be considered a precursor to electrical skyrmions.^[18] Finally,

The recent discovery of complex domain arrangements in nanoscale ferroelectrics has triggered an explosion in the search for exotic topologies that do not exist in the parent bulk materials.^[1] Structures such as vortex pairs,^[2] flux-closure

Dr. Q. Zhang, Dr. G. Liu, Prof. N. Valanoor
School of Materials Science and Engineering
The University of New South Wales
Sydney, New South Wales 2052, Australia
E-mail: nagarajan@unsw.edu.au

Dr. L. Xie
National Laboratory of Solid State Microstructures
and Department of Materials Science and Engineering
Nanjing University
Nanjing 210093, P. R. China

Dr. L. Xie
Department of Chemical Engineering and Materials Science
University of California
Irvine, CA 92697, USA

Dr. S. Prokhorenko
Theoretical Materials Physics
Q-MAT CESAM
University of Liège
Sart Tilman B-4000, Belgium

Dr. S. Prokhorenko, Dr. Y. Nahas, Prof. L. Bellaiche
Physics Department and Institute for Nanoscience and Engineering
University of Arkansas
Fayetteville, AR 72701, USA

Prof. X. Pan
Department of Chemical Engineering and Materials Science
University of California
Irvine, CA 92697, USA

Prof. X. Pan
Department of Physics and Astronomy
University of California
Irvine, CA 92697, USA

Prof. A. Gruverman
Department of Physics and Astronomy
University of Nebraska
Lincoln, NE 68588, USA

DOI: 10.1002/adma.201702375

their predicted size of ≈ 10 nm, almost 50 times smaller than their ferromagnet counterparts,^[16] makes them exciting candidates for investigation of emergent phenomena in nanoferroic materials, which has significant implications for applications in nanoelectronic sensors, memory, and logic devices and electro-mechanical systems.

Despite these potentially rich and rather promising physical properties, the experimental observation of ferroelectric bubble domains has thus far been elusive. Generally speaking, the most critical factor influencing the formation of ultrafine domain topologies is the strength of the residual depolarization field.^[14] If it is too high, which corresponds to the case of poorly screened polarization, it will simply break the ferroelectric state into the classical polydomain structure because the energy cost to create periodic domain walls is lower than that to maintain a uniform polarization.^[20] On the other hand, efficient polarization screening and considerable reduction of the residual depolarization field will favor a monodomain state. Theoretical models predict that polarization rotation – a key requirement for bubbles – would be only possible when it is energetically disadvantageous to create periodic domain walls.^[14,21,22] Thus, the critical condition for observation of bubble domains is the precise tuning of the residual depolarization field such that it induces toroidal/cycloidal topologies. In ultrathin films, this can be achieved by controlling the interplay between the thickness and electrical/mechanical boundary conditions of the ferroelectric layer.^[23]

In this report, we demonstrate nanoscale bubble domains in ultrathin (several nm thick) epitaxial $\text{PbZr}_{0.2}\text{Ti}_{0.8}\text{O}_3/\text{SrTiO}_3/\text{PbZr}_{0.2}\text{Ti}_{0.8}\text{O}_3$ (PZT/STO/PZT) sandwich heterostructures. The insertion of a STO dielectric spacer^[23–25] between two compressively strained (001) PZT ultrathin (≈ 3 nm) ferroelectric layers drives the formation of a distinctive speckled domain pattern consisting of nanoscale platelet-like domains (ranging from <10 to 20 nm in lateral size) embedded into the film matrix with uniform out-of-plane polarization, as revealed by high-resolution piezoresponse force microscopy (PFM). The STO spacer approach is chosen as it has been proven to be an innovative avenue to tune the depolarization field,^[3,23–26] and hence could be used to influence the nanoscale domain topology. Cross-sectional aberration-corrected scanning transmission electron microscopy (AC-STEM) mapping of the polarization displacements reveal that the ultrascale nanodomains (<10 nm) are spheroids with both out-of-plane and in-plane polarization components coupled with polarization rotation at the domain-matrix interface. We argue that these naturally forming domains satisfy the required topological conditions in three dimensions to be considered genuine bubble domains. It is found that the bubbles exhibit polarization rotation with mixed Néel–Bloch character to a point where distinguishing between a domain wall and domain becomes nearly impossible. The induced rotation must break the tetragonal symmetry of the parent PZT matrix thereby representing an entirely different ferroic phase. First-principles-based effective Hamiltonian simulations show that, depending on the depolarizing field strength, the polarization pattern in the sandwich heterostructures can have either labyrinthine, bubble, or monodomain structure. Time-dependent PFM investigations show

that the bubble domains easily transform to a labyrinthine state under repeated scanning. Hence, the bubble domains represent a transitional topological state at the interface between the two stable and more typical phases. Switching spectroscopic PFM loops find that starting from an as-grown state, the bubble domains show a steep rise in the electromechanical response under an initial applied electric field. However this increase is only temporary as the bubble domains undergo an irreversible electric field induced transformation to the cylindrical domain state. Repeated cycling is not able to recover to this enhanced state although the coercivity is found to be twice as small in comparison with the reference sample. Thus further understanding of the phase-field stability of these new type of domains is necessary to realize emergent bubble-domain-engineered electromechanical and electronic devices.

The (001)-oriented epitaxial PZT/STO/PZT sandwich heterostructures were fabricated on the $\text{La}_{0.67}\text{Sr}_{0.33}\text{MnO}_3$ (LSMO) electrode-buffered SrTiO_3 single crystalline substrates by pulsed laser deposition (PLD) (Figure 1a). (Details are given in the Experimental section.) The thickness of the PZT layers was fixed at 3 nm in each case, while the thickness of the STO spacer was varied from 1 to 4 unit cells (u.c.). Introduction of the STO spacer brings in a competition between long-range electrostatic coupling and short-range polarization screening requirements: as it disrupts the polarization continuity, it causes a local depolarization field.^[25] This would break the ferroelectric layers into the classic polydomain state.^[27] However, for certain thicknesses, the STO becomes polarized, which not only maintains the out-of-plane electrostatic coupling between the two ferroelectric layers, but also enhances the ferroelectric state.^[28] When an additional elastic degree of freedom (through epitaxial strain) is added, the appropriate strength of the depolarization field and consequently the required domain topology is attained.^[2]

Figure 1b shows an asymmetric reciprocal space map (ARSM) around the (103) peak of a representative sample from the series, namely a PZT/STO (2 u.c.)/PZT sample (hereafter referred to as PZT_2ucSTO). The detailed XRD analysis can be found in Section S1 (Supporting Information). Figure 1b displays a number of important features of this sample. First, the PZT/STO/PZT trilayer sample is fully constrained in the plane to the LSMO-buffered STO substrate, as attested by the fact that the crystal truncation rods for the ferroelectric heterostructure, the bottom LSMO electrode, and the STO substrate are aligned perfectly with each other along Q_x . Second, we do not observe satellite peaks for the PZT (103) peak along Q_x , confirming the absence of stripe domains; and third, there are no ferroelastic (90°) domains as there is no splitting in the PZT peak along Q_z . We point out that for ultrathin layers, extraction of the lattice parameters requires a comprehensive fitting procedure rather than simply identifying the 2θ position. Table 1 shows the individual lattice parameters for each sample obtained from various characterization methods (i.e., θ - 2θ XRD peak position, XRD fitting, and TEM). The trends in the lattice parameter are discussed further in the Supporting Information. It is important to point out that the STO spacer has an out-of-plane lattice parameter of 0.4 nm up to 3 u.c. spacer thickness, indicating that it is polarized due to the bottom PZT layer. On the other hand, the top and bottom PZT layers do not always have identical lattice parameters. The average out-of-plane lattice parameter for the

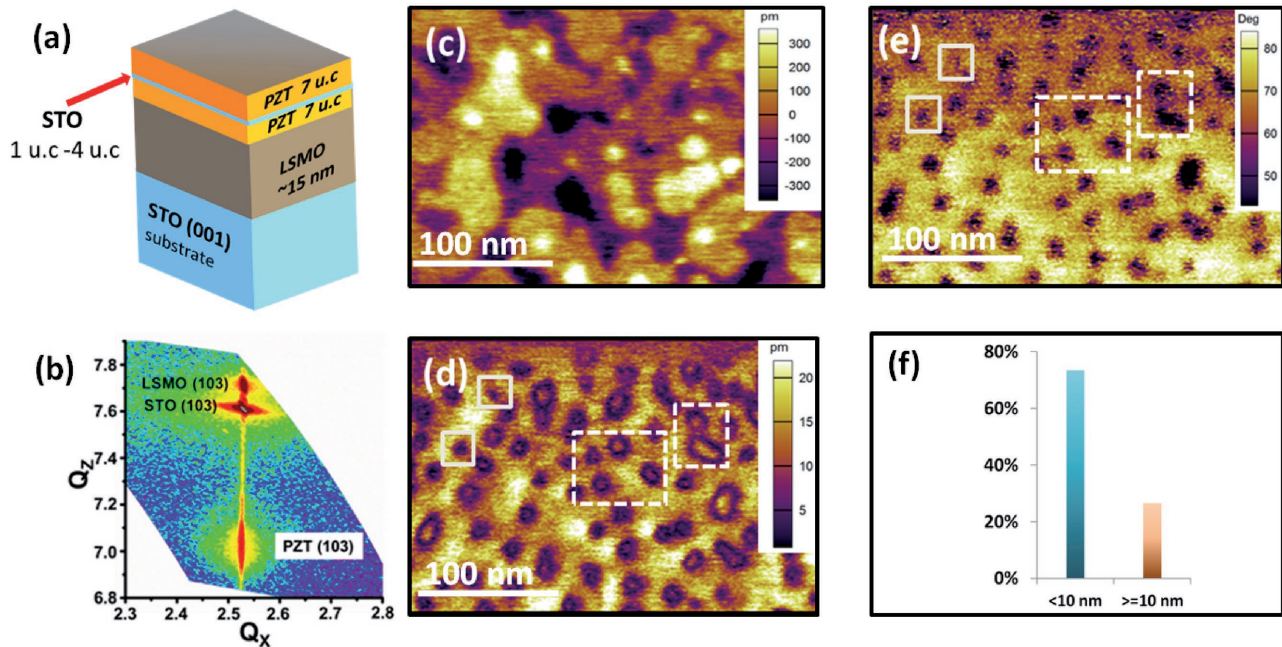


Figure 1. a) Schematic description of PZT/STO/PZT/LSMO/STO thin films; b) ARSM for (103) peak of PZT films with 2 u.c. STO spacer (PZT_2ucSTO film); c) topography, d) PFM amplitude, and e) PFM phase images of PZT_2ucSTO films, the scan size is 300 nm \times 200 nm, white dashed boxes indicate the cylindrical domains with clear domain walls and white boxes indicate the bubble domains with fuzzy domains walls; f) statistical size distribution of nanoscale domains in PZT_2ucSTO films, the lateral size histogram reveals \approx 70% of the domains are sub-10 nm regime.

PZT layers is 0.421 (\pm 0.002) nm (see Table 1 for details), in agreement with prior values reported for PLD-grown ultrathin $\text{PbZr}_{0.2}\text{Ti}_{0.8}\text{O}_3$ films.^[29] In summary, on a “bulk” scale the films are *c*-axis oriented with no discernible in-plane domains.

The domain structure for the PZT_2ucSTO sample was first examined using high-resolution dual amplitude resonance tracking (DART)-PFM. Figure 1c–e shows topographic, DART-PFM amplitude and phase images, respectively. They reveal a fascinating and complex polar nanodomain pattern. The entire film exhibits nanoscale platelet-like domains ranging from sub-10 to 20 nm in size. The DART-PFM amplitude (Figure 1d) reveals two significantly distinct domain topologies. Domains that are greater than \approx 10 nm in lateral size appear ring-like (marked by white dashed boxes), where the domain walls, which separate the up and down domain states, are clearly visible. As the lateral size of the domain is greater than the thickness of the trilayer structure, these are analogous to the classical cylindrical domains with domain walls normal to the bottom interface. Topologically these domains appear similar to those observed by Lichtensteiger et al. for 50 nm thick PbTiO_3 films

with an STO spacer,^[23] although their sizes were significantly larger, \approx 20–100 nm. While they were termed as “bubble” they are analogues of cylindrical domains, with several smaller cylinders perhaps merging anisotropically to result in the observed ovoid (pancake-like) shapes. The reduced domain size here (2–10 times smaller) is a direct consequence of the significantly lower film thickness.^[20,30]

More interesting are the ultras small domains (\ll 10 nm) (marked by white boxes in Figure 1d). These domains appear as dark spots since PFM cannot distinguish signals from the domain and the domain wall due to the PFM resolution limit. Therefore, it becomes impossible to discern their out-of-plane polarization state. This could easily stem from the fact that their size hampers clear rendering of the domain wall. However, this topology was typically found for domains that are smaller than or at the limit of the film thickness (\approx 7 nm). This observation thus offers a more tantalizing perspective: that these are truly spheroid bubble domains, possessing a topological state which has a continuous local polarization rotation manifested through mixed Néel–Bloch domain walls.

Table 1. *c* lattice parameters of PZT sandwich films with various STO spacer thicknesses.

Unit: Å	Fitting					XRD	TEM
	LSMO	Bottom PZT	STO	Top PZT	STO thickness (u.c.)	PZT (Avg)	PZT (Avg)
PZT_1ucSTO	3.86	4.29	4.00	4.24	1 \pm 0.5	4.22	
PZT_2ucSTO	3.86	4.29	4.00	4.23	2 \pm 0.5	4.22	4.24
PZT_3ucSTO	3.86	4.30	4.00	4.23	3 \pm 0.5	4.19	
PZT_4ucSTO	3.86	4.30	3.96	4.13	4 \pm 0.5	4.13	

Irrespective of their size, the corresponding PFM phase image (Figure 1e) shows that these nanodomains have a phase contrast that is different from the surrounding matrix and is less than 180° . This effect can be attributed to the weaker PFM signal of the bubble domains, which results from the summation of the various polarization projections on the vertical directions.^[31] These projections mapped out using transmission electron microscopy techniques are described in the next section. The histogram of the bubble domains size (Figure 1f) reveals that $\approx 70\%$ of the domains are less than 10 nm (i.e., ultrasmall domains). A $500 \times 500 \text{ nm}^2$ region PFM image of the same sample shown in Figure S2.1 (Supporting Information) confirms that the nanodomains with reduced PFM amplitude are uniformly distributed over the entire film matrix. The absence of any correlation between the spatial location of the nanodomains and the surface topography (Figure 1c; Figure S2.1a in the Supporting Information) rules out the possibility of imaging artifacts. Nanoscale domains were also observed for the PZT_1ucSTO and PZT_3ucSTO samples (shown in Figure S2.3 in the Supporting Information). On the other hand no bubbles were observed in the PZT_4ucSTO sample. This could be due to the decoupling between the two PZT layers separated by STO. The c lattice parameter of STO in PZT_4uc STO, extracted from XRD fitting, is approximately 0.396 nm, which is significantly smaller than that of PZT_1ucSTO, PZT_2ucSTO, PZT_3ucSTO films ($\approx 0.4 \text{ nm}$). This indicates that the STO spacer in PZT_4ucSTO is not polarized to the same extent as the thinner spacer samples, resulting in the disappearance of nanoscale domains. We also confirmed that a reference PZT sample ($\approx 7 \text{ nm}$ thick PZT films with no STO spacer) showed uniform domain contrast in PFM (Figure S2.4, Supporting Information). Annealing followed by AC PFM imaging (Supporting Information) experiments found that it was possible to erase the as-grown domains and nucleate several new domains spontaneously as a result of polarization relaxation. This proves the domains are not linked to the position or morphology of the STO layer underneath.

In order to shed light on the depth-resolved structure of the ultrasmall domains, not accessible by PFM, cross-sectional atomic-resolution scanning transmission electron microscopy (AC-STEM) imaging, along with direct polarization displacement mapping, was performed (the details are given in Section S3 in the Supporting Information). Here it must be borne in mind that the nanoscale domain size, coupled with their high density and random distribution, complicates analysis of the polarization displacement maps due to nearest neighbor interactions. To minimize this convolution due to nearest neighbor interactions, we found it necessary to examine the film through a selected area-by-area approach applied to two different images of the same sample. The full-scale

image seen in Section S3 (Supporting Information) reveals a highly intricate domain structure with significant disorder, unlike conventional $180^\circ c+/c-$ or $90^\circ c/a$ -domain patterns expected for a nominally tetragonal ferroelectric.

The cross-sectional STEM high angle annular dark-field (HAADF) imaging allowed us to identify regions that possess a distinct bubble topology. In Figure 2a,b, we compare the matrix regions with the ultrasmall domains, respectively. Figure 2a shows that the matrix is predominantly poled downwards, in agreement with the DART-PFM data. On the other hand, a dramatic difference is seen for the region bound by the blue circle in Figure 2b, with net out-of-plane polarization pointing upwards. It is nearly impossible to discern between a domain and a domain wall in this region. Such a diffuse arrangement is in complete contrast to the well-defined traditional 180° or 90° domain structures found for tetragonal PZT, i.e., but in close resemblance to dipolar incommensurate nanoregions in ultrathin PbTiO_3 films^[7] where the apparently disordered state forms as a consequence of the induced depolarization field at a tricritical Lifshitz point.^[22] Even though at first glance the polarization seems random, a closer inspection reveals subtle topological features with a rich array of polar modulations, ranging from pure undulations (see bottom interface) to kinks and ripples. At several locations the dipole arrows propagate away from a disclination point, following the topological arrangement of center-type domains.^[32] Furthermore, they have an in-plane direction that has long-range order and predominantly poled to the left, which is confirmed by lateral-PFM scans (see Section S2 in the Supporting Information). Remarkably, the

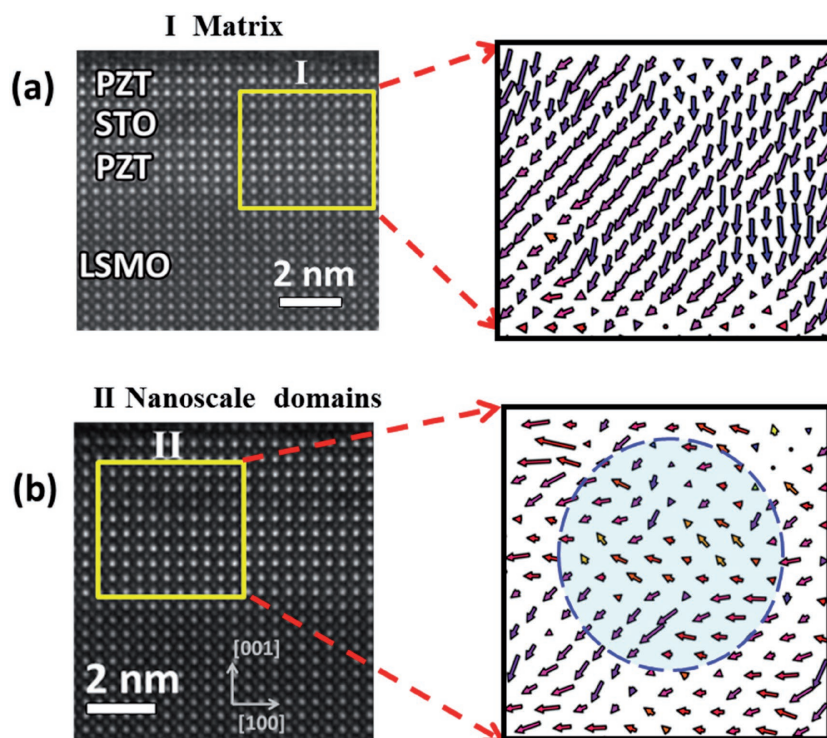


Figure 2. Cross-sectional STEM high angle annular dark-field (HAADF) images of PZT_2ucSTO films (left) and corresponding polarization displacement mapping for zoom in area (right) of regions with two distinct topologies each representing the a) matrix and b) a bubble domain.

polarization profile at the bottom interfaces for Figure 2a,b is strikingly similar to those predicted by Kornev et al.^[14] during the formation of bubble domains. Geometric phase analysis (see the Supporting Information) also found that the shear strain component and the rotation angle continuously change across the film, indicating a subtle distortion and rotation of the lattice between different regions. Furthermore, they do not reveal point or line defects concomitant with the bubble density – thus precluding microstructural defects as simply the origin of the bubble domain contrast.

We found that such nanodomains are dispersed over the entire cross-section of the film (see Section S3 in the Supporting Information) with size and spacing that closely matched the PFM images for the ultrasmall domains. For domain sizes in the sub-10 nm range, it is known that the energy cost to create a domain wall is prohibitively high and, hence, the gradient term related to the energy required to rotate or tilt the polarization in order to minimize depolarization field^[33] becomes dominant. This results in the precession of the polarization with an out-of-plane component as it curls around a disclination center as well as stabilization of incommensurate phases.^[22] Indeed, first-principles-based computations predict a similar domain pattern, which consists of the spontaneously formed bubble domains dispersed within a matrix of typically *c*-axis oriented ferroelectric domains.^[14] Although there is not enough evidence here to categorically claim continuous precession of the polarization vector in all three directions (i.e., a hedgehog polarization state), a combination of PFM and AC-STEM image analysis nevertheless suggests nucleation of ferroelectric bubble domains in the ultrathin PZT film.

To understand the formation of such bubble domains, we have performed Monte Carlo simulations using the effective Hamiltonian model from ref.[16] for tetragonal $\text{PbZr}_{0.4}\text{Ti}_{0.6}\text{O}_3$ films.^[34] The total energy can be expressed as

$$E_{\text{tot}} = E_{\text{eff}}(\{u_i\}, \{v_i\}, \{\sigma_i\}, \eta) - 2\pi\beta \frac{Z^2}{a^3 \epsilon_{\infty}} \langle u_{j,z} \rangle_s \sum_i u_{i,z} \quad (1)$$

where the first term, E_{eff} , describes the energy of an epitaxial ferroelectric film under ideal open circuit (OC) boundary conditions.^[16] The relevant optical phonon modes are parametrized via the local-mode variables u_i , each proportional to a local electric dipole of the *i*th unit cell, while vectors v_i represent acoustic phonon branches. E_{eff} explicitly takes into account various interactions that affect the dipolar structure. Such interactions include coupling of local dipoles u_i to acoustic phonons, effects of chemical disorder (variables $\{\sigma_i\}$ describe the distribution of Zr and Ti atoms), as well as electrostrictive coupling of each u_i to the homogeneous strain tensor η . The η tensor has three components (in Voigt notation) that are fixed during the simulations ($\eta_6 = 0$, and $\eta_1 = \eta_2 = \delta$, with δ being the epitaxial misfit strain between $\text{PbZr}_{0.4}\text{Ti}_{0.6}\text{O}_3$ and SrTiO_3), while components η_3 , η_4 , and η_5 are allowed to relax in accordance with elastic boundary conditions for epitaxial (001) films. Finally, E_{eff} also includes the energy of depolarizing field stemming from long-range electrostatic interactions between local dipoles. In particular, the simulation supercell is periodic only along [100] and [010] pseudo-cubic directions and has a finite thickness along the [001] direction. Moreover, the electric boundary

conditions at the film's surface correspond to an interface of a ferroelectric medium with vacuum. In other words, the local dipoles u_i vanish outside of the film leading to an accumulation of a bound electric charge at the interface, whose density is proportional to the average [001] component of local modes $\langle u_{j,z} \rangle_s$ within the interface ferroelectric layer.

The second term describes the effect of degree of polarization screening. Specifically, it removes a fraction β of the energy related to the depolarizing field and hence, the value of β tells what percentage of the surface charge density is screened. As such, $\beta = 1$ corresponds to the case of 100% screening (ideal short circuit boundary conditions), while $\beta = 0$ corresponds to an absence of screening charges, or equivalently OC boundary conditions.

At room temperature ($T = 300$ K), our simulations show that several distinct dipolar phases can be stabilized, depending on the value of β . Specifically, below $\beta = 0.871$ the equilibrium structures can be described as a labyrinth domain pattern (phase L in Figure 3a and its inset). Upon reaching $\beta = 0.871$, the system transitions to a state characterized by the occurrence of a significant number of bubble domains (phase B in Figure 3a) embedded in the homogeneously polarized ferroelectric matrix. Finally, increasing β above 0.895 results in a transition to a mono-domain state (phase M of Figure 3a). Note that at low temperatures, our simulations yield only a transition from the striped domain pattern to the mono-domain state upon increasing the value of β . Stability of bubble domains, therefore, requires specific combinations of temperature and electrical boundary conditions.

Strikingly, the obtained sequence of phase transitions at room temperature, i.e., from stripe to bubble to mono-domain state upon increasing β (Figure 3a), is similar to that earlier predicted for PZT thin films at constant strength of the surface charge compensation ($\beta = 0.81$), but under varying magnitude of an external electric field^[16] applied along the [001] pseudo-cubic direction. This is indeed expected since increasing the screening strength β , or analogously, applying an external bias electric field, contributes to effectively reduce the depolarizing field.

The calculated dipolar structure (already shown in Figure 3b) reveals further key details. The local dipoles point in a direction opposite to the polarization of surrounding medium. Note that the employed Hamiltonian is invariant with respect to inversion of the *z*-axis (interfaces of the film with vacuum and the substrate are treated equivalently) and hence the polarization of the bubble, while being opposite to that of the matrix, can be directed either along [001] or $[00\bar{1}]$ pseudocubic direction. Upon moving away from the bubble core within the (001) plane, we find that the local dipoles rotate towards the direction of polarization of the matrix in a mixed Bloch-like/Néel-like manner. Figure 3c shows an example of Bloch-like rotation pattern obtained from Monte Carlo simulations that can occur upon radially traversing the bubble domain. Here, the dipoles rotate in the plane perpendicular to the chosen radial path direction. The same bubble domain can also exhibit a Néel-like rotation pattern along another radial direction (see Figure 3d) and in this case, the dipoles rotate in a cycloidal manner, developing non-zero projection along the considered path. Recently, Néel or Bloch type domain walls were found for $\text{PbZr}_x\text{Ti}_{1-x}\text{O}_3$

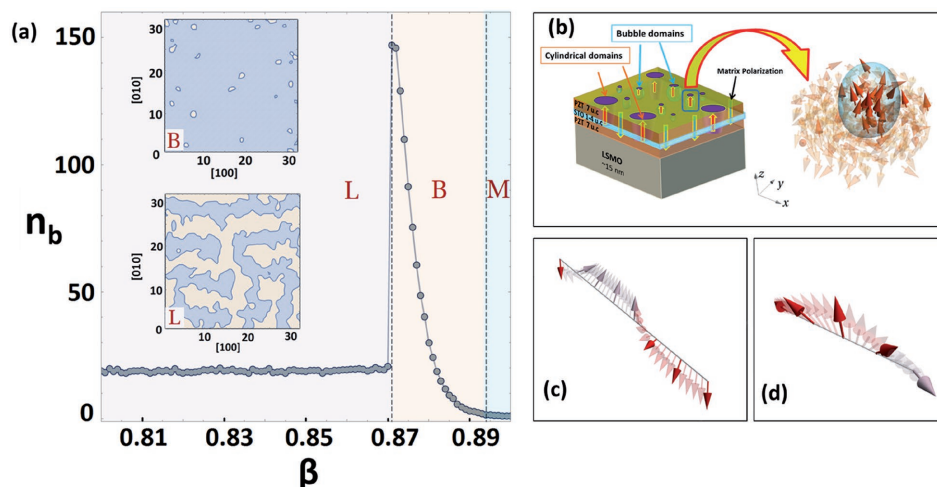


Figure 3. a) Calculated room temperature ($T = 300$ K) phase diagram of $\text{PbZr}_{0.4}\text{Ti}_{0.6}\text{O}_3$ films with varying strength of interfacial screening described by the phenomenological screening parameter β . Data points correspond to the calculated equilibrium number of isolated bubble domains (n_b) and allow to distinguish between three phases: the labyrinthine domains (L), bubble domains state (B), and the monodomain state (M). The two inset figures show the regions corresponding to up and down polarization domains within the B phase ($\beta = 0.873$) and L phase ($\beta = 0.870$), respectively, for a (001) plane of the supercell. b) Schematic description of nanoscale domains inside the films, the blue box indicates the bubble domains and the zoom-in figure illustrates the calculated dipolar structure of this bubble domain obtained from Monte Carlo simulations. c) Bloch-like and d) Neel-like character of dipole rotation upon radially traversing the bubble. Cartesian x , y , and z axes coincide with [001], [010], and [001] pseudocubic crystallographic directions. Orange to purple color gradient denotes the variation of the z Cartesian component of local dipoles.

single crystals^[5] where their occurrence was attributed to a structural phase coexistence/competition effect at the MPB.^[5] Since the PZT composition used here is well into the tetragonal part of the PZT phase diagram, we believe that the underlying cause here is more closely related dipolar incommensuration driven by depolarization field.^[7] Again the high density of nanodomains in close proximity to each other precludes us from capturing mixed rotational walls in a clear manner. We are working towards strategies which will allow us to control the bubble spacing such that an isolated bubble can be studied.

We now attempt to address a question of why imaging of ferroelectric bubble domains has remained elusive despite the fact that theoretical predictions go as far back as 2004.^[14] **Figure 4** shows a series of time-dependent DART-PFM scans of the PZT_1ucSTO sample. Tiny bubble domains (at the upper limit of PFM resolution) without clear domain boundaries with an average diameter of approximate 7–8 nm (marked by arrows in Figure 4a) are observed in the first scan. We observe that with under successive imaging scans (using 200 mV imaging AC bias), the bubbles first start to transform into cylindrical domains, the cylindrical domains then coalesce, and eventually the whole region that originally had bubble domains transforms into the well-known labyrinth structure (Figure 4b–e). This entire sequence is schematically depicted in Figure 4f. The similar behavior has been observed in other PZT/STO/PZT sandwich structures with different STO thicknesses (see Figure S4 in the Supporting Information). It can be concluded that the bubble domains are stable only within a very narrow range of boundary conditions determined by a balance between elastic and polarization energy terms. Even the slightest of external forces (for example, the tip-induced pressure) is enough to distort them. It is very likely that bubble domains are the first step in any ferroelectric domain switching process but are kinetically unstable, and hence are not easily imaged. Indeed, this feature

is captured by our theoretical model where the switching process is considered as going from right to left in Figure 3a.^[14] On the other hand, the result of such topological transition – the stripe or labyrinth domain structure – is extremely stable, which explains why it could be easily visualized as has been demonstrated on numerous occasions.

Previous computations^[14] also predicted that such topological structures may have enhanced piezoelectric coefficients due to the electric-field induced rotation of the polarization from in-plane to out-of-plane direction.^[35] To test if the bubbles here can potentially be exploited for their polarization rotation response, switching spectroscopic PFM hysteresis behavior of the PZT_2ucSTO sample was investigated.^[36] The PFM data for our bubble domain (**Figure 5a**) yield fundamental insight into their stability under an external electric field. Particularly by looking at the individual segments, especially for the very first cycle one can identify subtle changes that take place as a function of the hysteresis drive sequence. In Figure 5a, the first segment of the first cycle (0 to –4 V, top loop labeled as “1”), plotted in black, shows a steep incline in the PFM amplitude signal. We attribute this continuously rising PFM amplitude to progressive increase in the degree of polarization rotation within the individual bubble domain due to the increasing electric field. The response rises to a value that is nearly 300% of the virgin state. Note that the domains in Figure 1d do not show such a high amplitude contrast as found in Figure 5a as they are imaged as-grown under small-signal AC bias conditions (the first data point of the segment 1). However applying this negative bias causes the bubble domains to undergo an electric-field induced phase transformation to the cylindrical domain state. Figure 5b,c shows the before and after PFM phase images of a bubble domain surface, respectively. It is evident that once a bias of –4 V is applied, the area under the tip that was previously a bubble is now fully converted to

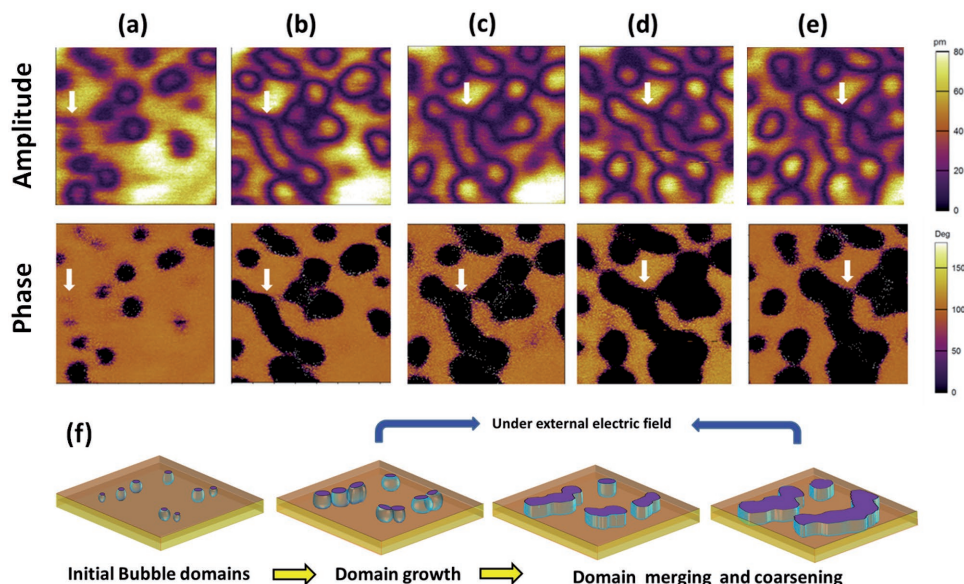


Figure 4. a–e) PFM amplitude and phase images of PZT_1ucSTO film showing its domain evolution process under an AC amplitude of 200 mV for successive five scans. White arrows indicate the location of a single bubble domain. f) Schematic of the bubble domain evolution process.

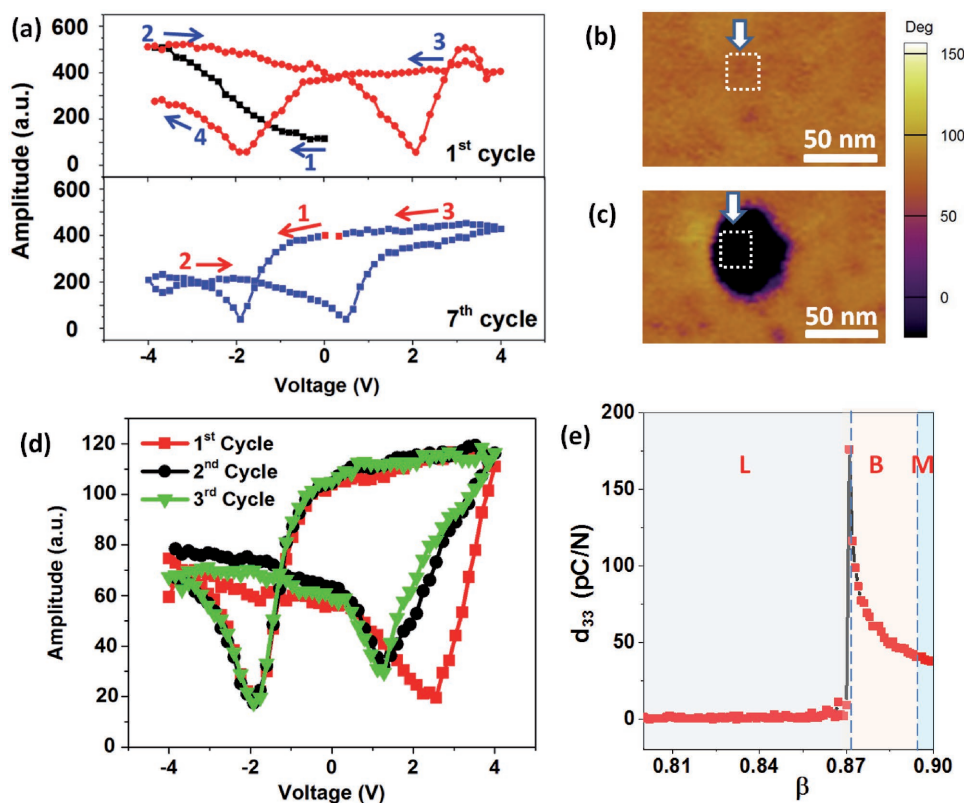


Figure 5. Local PFM hysteresis loops of a) PZT_2uc STO film acquired at bubble domain regions. Note the steep incline in the first part of the cycle (black) which signifies the bubble domain is undergoing polarization rotation. Once maximum voltage is reached the d_{33} response begins to rapidly decline (segment indicated as 2 in top part of panel (a)). Now the bubble is converted to a cylindrical state, and thus the d_{33} does not recover to the maximum value on the return path. Now even after 7 cycles it remains low. Phase images of local bubble regions b) before and c) after PFM hysteresis loop measurement, white arrows and dashed boxes indicate the tip position where DC voltage applied. In contrast the PZT reference film d) remains constant with no such progressive changes. e) The calculated d_{33} piezoelectric coefficient of $\text{PbZr}_{0.4}\text{Ti}_{0.6}\text{O}_3$ films with varying strength of interfacial screening described by the phenomenological screening parameter β .

a cylindrical domain, as confirmed by morphology change and the phase difference between the bubble domain and matrix, which is now 180° (Figure 5c). We can also infer this by examining the return segment of the first cycle (-4 V to 0, labeled 2 in top part of Figure 5a), where the drop in the PFM amplitude with decreasing bias is at a slope markedly different from the initial rise. Critically the next segment of the hysteresis loop, under positive drive bias is no longer able to reproduce the positive steep incline observed for the very first segment 1. This strongly suggests that the bubble domains have undergone an irreversible phase transition, confirmed by the failure to be recovered even after repeated cycling (bottom part of Figure 5a). No such changes are found for the reference sample (see Figure 5d), where the loop shape remains approximately the same for each cycle. Finally we note the coercive voltage for the spacer sample after switching to the cylindrical state is lower than the reference sample, in agreement with our previous report that revealed the positive effect of ultrathin spacers.^[26]

Theoretical simulations further support these observations. Figure 5e plots the calculated d_{33} piezoelectric coefficient as a function of the screening parameter β (i.e., an internal field). It shows a peak in d_{33} of 170 pm V^{-1} at $\beta = 0.871$, corresponding to transition from the labyrinth to the nanobubble phase indicating the strong coupling between the strain and polarization degrees of freedom in such bubble domains. In fact, this behavior is reminiscent of a ferroelectric with morphotropic phase boundary composition, the difference here being that instead of composition^[37] or strain-based^[38] phases, the competition between ultrafine domain topology variants gives rise to a giant electromechanical response. However to practically exploit this enhancement the external stimulus must permit repeated straddling across the phase boundary, such that one can retain that state reversibly. Only then will the bubble domains show immense potential for nanoscale electromechanical devices. We are currently conducting investigations to explore this point further.

Our observations raise a number of key questions. For example, given the tremendous improvements in both PFM and STEM techniques, are there other systems where such bubble domains could exist? Would it be possible to nucleate these bubble domains so as to generate ordered, regular periodic arrays which can be moved along an electrode in a controlled fashion similar to the experiments on magnetic domain-wall register,^[39] magnetic race track memory^[40] and skyrmion.^[12,41] Given that recent theoretical computations predicted the existence of topological defects in relaxor ferroelectrics,^[42] it would be interesting to see if the bubble domains were akin to polar nanoregions in relaxors in terms of their fundamental dielectric behavior. Although we have not yet observed domain-wall conduction in the present system, we expect that the design strategy use here could be applied to other multiferroics (such as BiFeO_3) where domain-wall conduction^[43] has fuelled an explosion of ideas. The idea that we could employ such cycloidal domain topologies in tunnel junction devices^[44] has already opened new paradigms in “nanoferronics.”^[7] Addressing these questions will stimulate further studies of novel emerging domain patterns in nanoscale ferroelectrics.

In summary, we have reported the observation of a new type of ferroelectric nanodomains – bubble domains – in ultrathin

epitaxial $\text{PbZr}_{0.2}\text{Ti}_{0.8}\text{O}_3$ ferroelectric sandwich structures with dielectric spacers. First-principles simulations show that the bubble domains can be stabilized only within a very narrow range of the electric and elastic boundary conditions. This is indeed observed experimentally, where the bubbles easily transform into a labyrinthine (stripe) domain structure by simply continuous scanning of the PFM tip. Innovative strategies are required to stabilize the bubble domains under electric field, which would make them appealing for advanced electromechanical devices.

Experimental Section

Film Growth: Epitaxial $\text{PbZr}_{0.2}\text{Ti}_{0.8}\text{O}_3/\text{SrTiO}_3/\text{PbZr}_{0.2}\text{Ti}_{0.8}\text{O}_3$ thin film heterostructures were deposited on (001)-oriented stepped SrTiO_3 substrates (Shinkosha Co., Ltd, Japan) with 15 nm buffered LSMO electrode using a pulsed laser deposition system (Neocera Co., Ltd, USA). The thickness of the top and bottom PZT layers were set to 3 nm each while the STO layer varies from 1 to 4 u.c. in thickness. The thickness of the PZT and the STO spacer layers was calibrated using a custom-made program based on X-ray reflectivity fitting^[45] and ex situ reflective high energy electron diffraction oscillations (the details are presented in Section S1 in the Supporting Information). A reference PZT sample (without STO spacer) with a total thickness of approximately 6 nm was grown on STO (001) substrate with 15 nm buffered LSMO. For the growth of all the layers, the ambient oxygen pressure was maintained at 100 mTorr. Substrate–target distance was approximately 15 cm and laser fluence $2\text{--}2.5 \text{ J cm}^{-2}$. The LSMO buffer layers were prepared at 800°C with a laser repetition rate of 5 Hz, while both the PZT and STO layers were grown at 700°C at a laser repetition rate of 3 Hz. After deposition, the samples were cooled to room temperature at $20^\circ\text{C min}^{-1}$ in 450 Torr of oxygen.

Scanning Probe Microscopy: Ferroelectric domains of PZT thin films were observed using a commercial scanning probe microscope (Cypher, Asylum Research, US) using the dual AC resonance tracking (DART) mode. Conductive Cr/Pt coated silicon cantilevers (BudgetSensors ElectricMulti75-G, Bulgaria) were used for both PFM imaging and PFM hysteresis loop measurement. The typical tip radius is less than 25 nm and the force constant is $\approx 3 \text{ N m}^{-1}$. PFM images of nanoscale domains were captured using AC amplitude ranging from 100 to 600 mV. The domain size and size distribution were measured using the Gwyddion software to identify the bubble domain diameters. Specifically, the sizes of irregular domains were calculated as the average of two in-plane perpendicular axes.

Transmission Electron Microscopy: STEM HAADF experiments were carried out on a FEI Titan 60–300 microscope at Nanjing University. The microscope is equipped with double aberration correctors and its resolution in STEM mode is $\approx 0.6 \text{ \AA}$. The accelerating voltage, convergence angle of the incident electrons, and the collection angle for HAADF imaging are 300 kV, 22 mrad and 79–200 mrad, respectively. Geometric phase analysis (GPA) and electron energy loss spectroscopy (EELS) were performed to identify the location of the interfaces. GPA was done using the commercial software package DigitalMicrograph with plug-in FRWRtools. Two diffractogram spots, i.e., $[101]^*_{\text{PC}}$ and $[10\bar{1}]^*_{\text{PC}}$, were selected and the resolution was $\approx 1 \text{ nm}$. The strain tensor was then calculated by taking the lower cubic LSMO as the reference. STEM EELS experiments were performed with 300 kV electrons and a convergence angle of $\approx 30 \text{ mrad}$. The collection angle and energy dispersion for EELS acquisitions were 36 mrad and 1 eV per channel, respectively. For each pixel, a dwell time of 0.1 s was used to acquire the spectra. During the acquisition, both the zero-loss peaks and the core-loss spectra were recorded simultaneously in DualEELS mode. The postprocessing of the spectra, i.e., alignment of spectra by zero-loss peaks and removal of the backgrounds in core-loss spectra, was carried out in the commercial software package DigitalMicrograph.

Computational Simulations: The dimension of the simulation supercell was chosen to be $32 \times 32 \times 5$ u.c., and periodic boundary conditions were considered along pseudo-cubic [100] and [010] directions mimicking the geometry of epitaxial films. The effective Hamiltonian employed in this study is that of ref. [46]. Its total internal energy has the form

$$\varepsilon_{\text{tot}}(\{\mathbf{u}_i\}, \{\sigma_i\}, \{\mathbf{v}_i\}, \eta) = \varepsilon_{\text{Heff}}(\{\mathbf{u}_i\}, \{\sigma_i\}, \{\mathbf{v}_i\}, \eta) + \beta \sum_i \langle \mathbf{E}_{\text{dep}} \rangle \cdot \mathbf{Z}^* \mathbf{u}_i - \sum_i \mathbf{E} \cdot \mathbf{Z}^* \mathbf{u}_i \quad (2)$$

where \mathbf{u}_i is the local soft mode in the unit cell i of the film. The product of \mathbf{u}_i with the effective charge \mathbf{Z}^* yields the local electrical dipole in this cell. The variables σ_i characterize the atomic configuration of the alloy. Specifically, it characterizes the atomic distribution of the mixed B-site sublattice with $\sigma_i = 1$ ($\sigma_i = -1$) for Ti (Zr) atom. The $\{\mathbf{v}_i\}$ are the inhomogeneous strain-related variables inside the film and η is the homogeneous strain tensor. Since we consider epitaxial (001) films, three of the six components of η (in Voigt notation) are frozen as done in ref. [46]. $\varepsilon_{\text{Heff}}$ denotes the alloy effective Hamiltonian (intrinsic energy of the ferroelectric film). Its expression is given in ref. [46], where for the treatment of dipole–dipole interactions we use the methodology described in ref. [21] for thin films under ideal OC conditions. Such electrical boundary conditions naturally lead to the existence of a maximum depolarizing field (denoted by $\langle \mathbf{E}_{\text{dep}} \rangle$) inside the film, corresponding to the situation where dipoles point along the [001] direction. The second term, $\beta \sum_i \langle \mathbf{E}_{\text{dep}} \rangle \cdot \mathbf{Z}^* \mathbf{u}_i$, represents the screening of $\langle \mathbf{E}_{\text{dep}} \rangle$ whose strength is captured by the phenomenological β parameter. Specifically, the residual depolarizing field, resulting from the combination of the first and second terms, has a magnitude equal to $(1 - \beta) \mathbf{E}_{\text{dep}}$. Therefore $\beta = 0$ corresponds to ideal OC boundary conditions, while $\beta = 1$ represents the ideal short-circuit conditions with vanishing depolarizing field. Finally, the third term embodies the effect of an external homogeneous electric field \mathbf{E} . The parameters entering in $\varepsilon_{\text{Heff}}$ are derived from first principles. The Monte Carlo simulations were performed using Metropolis annealing algorithm from 2000 down to 50 K for varying β values. At each temperature and chosen β the calculations consisted of 100 000 sweeps thermalization followed by 100 000 averaging sweeps.

Supporting Information

Supporting Information is available from the Wiley Online Library or from the author.

Acknowledgements

Q.Z. and L.X. contributed equally to this work. The research at University of New South Wales (UNSW) was supported by an Australian Research Council (ARC) Discovery Project. The TEM work at University of California-Irvine (L.X. and X.Q.P.) was supported by the Department of Energy (DOE) under grant DE-SC0014430 and the National Science Foundation (NSF) under grant numbers DMR-1506535 and DMR-1420620. The work at Nanjing University (L.X. and X.Q.P.) was supported by the National Basic Research Program of China (No. 2015CB654900) and National Natural Science Foundation of China (Nos. 51302132 and 11474147). The work at the University of Nebraska-Lincoln (A.G.) was supported by the National Science Foundation (NSF) through Materials Research Science and Engineering Center (MRSEC) under grant number DMR-1420645 and by the Center for Nanoferroic Devices (CNFD), a Semiconductor Research Corporation Nanoelectronics Research Initiative (SRC-NRI) under Task ID 2398.002, sponsored by NIST and the Nanoelectronics Research Corporation (NERC). S. P. and L.B. acknowledge the DARPA Grant No. HR0011-15-2-0038 (under the MATRIX program). S. P. acknowledges the support of University of Liège and the EU in the context of the FP7-PEOPLE-COFUND-BelPD project. Y.N. acknowledges the ARO grant W911NF-16-1-0227. The authors also acknowledge discussions and constructive criticisms from Celine Lichtensteiger (University of Geneva), Javier Junquera (University of Santander), and Marin Alexe (University of Warwick).

Conflict of Interest

The authors declare no conflict of interest.

Keywords

aberration-corrected scanning transmission electron microscopy, nanoscale bubble domains, Néel–Bloch domain walls, piezoresponse force microscopy, ultrathin ferroelectric films

Received: April 28, 2017

Revised: July 10, 2017

Published online: October 24, 2017

- [1] J. Seidel, R. K. Vasudevan, V. Nagarajan, *Adv. Electron. Mater.* **2016**, 2, 1500292.
- [2] A. K. Yadav, C. T. Nelson, S. L. Hsu, Z. Hong, J. D. Clarkson, C. M. Schlepuetz, A. R. Damodaran, P. Shafer, E. Arenholz, L. R. Dedon, D. Chen, A. Vishwanath, A. M. Minor, L. Q. Chen, J. F. Scott, L. W. Martin, R. Ramesh, *Nature* **2016**, 530, 198.
- [3] Y. L. Tang, Y. L. Zhu, X. L. Ma, A. Y. Borisevich, A. N. Morozovska, E. A. Eliseev, W. Y. Wang, Y. J. Wang, Y. B. Xu, Z. D. Zhang, S. J. Pennycook, *Science* **2015**, 348, 547.
- [4] a) R. G. P. McQuaid, L. J. McGilly, P. Sharma, A. Gruverman, J. M. Gregg, *Nat. Commun.* **2011**, 2, 404; b) R. G. P. McQuaid, A. Gruverman, J. F. Scott, J. M. Gregg, *Nano Lett.* **2014**, 14, 4230; c) C. T. Nelson, B. Winchester, Y. Zhang, S. J. Kim, A. Melville, C. Adamo, C. M. Folkman, S. H. Baek, C. B. Eom, D. G. Schlom, L. Q. Chen, X. Q. Pan, *Nano Lett.* **2011**, 11, 828.
- [5] X. K. Wei, C. L. Jia, T. Sluka, B. X. Wang, Z. G. Ye, N. Setter, *Nat. Commun.* **2016**, 7, 12385.
- [6] B. J. Rodriguez, X. S. Gao, L. F. Liu, W. Lee, I. I. Naumov, A. M. Bratkovsky, D. Hesse, M. Alexe, *Nano Lett.* **2009**, 9, 1127.
- [7] J. J. P. Peters, G. Apachitei, R. Beanland, M. Alexe, A. M. Sanchez, *Nat. Commun.* **2016**, 7, 13484.
- [8] B. V. Van Aken, J. P. Rivera, H. Schmid, M. Fiebig, *Nature* **2007**, 449, 702.
- [9] Y. N. Geng, N. Lee, Y. J. Choi, S. W. Cheong, W. D. Wu, *Nano Lett.* **2012**, 12, 6055.
- [10] N. Balke, B. Winchester, W. Ren, Y. H. Chu, A. N. Morozovska, E. A. Eliseev, M. Huijben, R. K. Vasudevan, P. Maksymovych, J. Britson, S. Jesse, I. Kornev, R. Ramesh, L. Bellaiche, L. Q. Chen, S. V. Kalinin, *Nat. Phys.* **2012**, 8, 81.
- [11] E. A. Eliseev, P. V. Yudin, S. V. Kalinin, N. Setter, A. K. Tagantsev, A. N. Morozovska, *Phys. Rev. B* **2013**, 87, 054111.
- [12] S. Woo, K. Litzius, B. Kruger, M. Y. Im, L. Caretta, K. Richter, M. Mann, A. Krone, R. M. Reeve, M. Weigand, P. Agrawal, I. Lemesch, M. A. Mawass, P. Fischer, M. Klau, G. Beach, *Nat. Mater.* **2016**, 15, 501.
- [13] I. I. Naumov, L. Bellaiche, H. X. Fu, *Nature* **2004**, 432, 737.
- [14] I. Kornev, H. X. Fu, L. Bellaiche, *Phys. Rev. Lett.* **2004**, 93, 196104.
- [15] According to ref. [16] each nanodomain is terminated at the surface by a large in-plane and small out-of-plane polarization to minimize the electrostatic energy.
- [16] B. K. Lai, I. Ponomareva, I. I. Naumov, I. Kornev, H. X. Fu, L. Bellaiche, G. J. Salamo, *Phys. Rev. Lett.* **2006**, 96, 137602.
- [17] a) P. Milde, D. Kohler, J. Seidel, L. M. Eng, A. Bauer, A. Chacon, J. Kindervater, S. Muhlbauer, C. Pfleiderer, S. Buhardt, C. Schutte, A. Rosch, *Science* **2013**, 340, 1076; b) S. Seki, X. Z. Yu, S. Ishiwata, Y. Tokura, *Science* **2012**, 336, 198.

- [18] Y. Nahas, S. Prokhorenko, L. Louis, Z. Gui, I. Kornev, L. Bellaiche, *Nat. Commun.* **2015**, *6*, 8542.
- [19] A. P. Malozemoff, J. C. Slonczewski, R. Wolfe, *Magnetic Domain Walls in Bubble Materials*, Academic Press, Inc, New York **1979**.
- [20] M. E. Lines, A. M. Glass, *Principles and Applications of Ferroelectrics and Related Materials*, Oxford University Press, Oxford **1977**.
- [21] I. Ponomareva, I. I. Naumov, I. Kornev, H. Fu, L. Bellaiche, *Phys. Rev. B* **2005**, *72*, 140102.
- [22] H. Pottker, E. K. H. Salje, *J. Phys.: Condens. Matter* **2016**, *28*, 075902.
- [23] C. Lichtensteiger, S. Fernandez-Pena, C. Weymann, P. Zubko, J. M. Triscone, *Nano Lett.* **2014**, *14*, 4205.
- [24] E. Bousquet, M. Dawber, N. Stucki, C. Lichtensteiger, P. Hermet, S. Gariglio, J. M. Triscone, P. Ghosez, *Nature* **2008**, *452*, 732.
- [25] P. Zubko, N. Jecklin, A. Torres-Pardo, P. Aguado-Puente, A. Gloter, C. Lichtensteiger, J. Junquera, O. Stephan, J. M. Triscone, *Nano Lett.* **2012**, *12*, 2846.
- [26] a) H. Lu, X. Liu, J. D. Burton, C. W. Bark, Y. Wang, Y. Zhang, D. J. Kim, A. Stamm, P. Lukashev, D. A. Felker, C. M. Folkman, P. Gao, M. S. Rzechowski, X. Q. Pan, C. B. Eom, E. Y. Tsymbal, A. Gruverman, *Adv. Mater.* **2012**, *24*, 1209; b) G. Q. Liu, J. S. Chen, C. Lichtensteiger, J. M. Triscone, P. Aguado-Puente, J. Junquera, V. Nagarajan, *Adv. Electron. Mater.* **2016**, *2*, 1500288; c) Y. H. Chu, Q. He, C. H. Yang, P. Yu, L. W. Martin, P. Shafer, R. Ramesh, *Nano Lett.* **2009**, *9*, 1726.
- [27] a) C. Thompson, D. D. Fong, R. V. Wang, F. Jiang, S. K. Streiffer, K. Latifi, J. A. Eastman, P. H. Fuoss, G. B. Stephenson, *Appl. Phys. Lett.* **2008**, *93*, 182901; b) G. Catalan, H. Bea, S. Fusil, M. Bibes, P. Paruch, A. Barthelemy, J. F. Scott, *Phys. Rev. Lett.* **2008**, *100*, 027602.
- [28] V. R. Cooper, K. Johnston, K. M. Rabe, *Phys. Rev. B* **2007**, *76*, 020103.
- [29] C. L. Jia, V. Nagarajan, J. Q. He, L. Houben, T. Zhao, R. Ramesh, K. Urban, R. Waser, *Nat. Mater.* **2007**, *6*, 64.
- [30] R. C. Miller, G. Weinreich, *Phys. Rev.* **1960**, *117*, 1460.
- [31] J. Chen, A. Gruverman, A. N. Morozovska, V. Nagarajan, *J. Appl. Phys.* **2014**, *116*, 124109.
- [32] R. K. Vasudevan, Y. C. Chen, H. H. Tai, N. Balke, P. P. Wu, S. Bhattacharya, L. Q. Chen, Y. H. Chu, I. N. Lin, S. V. Kalinin, V. Nagarajan, *ACS Nano* **2011**, *5*, 879.
- [33] G. Catalan, A. Lubk, A. H. G. Vlooswijk, E. Snoeck, C. Magen, A. Janssens, G. Rispens, G. Rijnders, D. H. A. Blank, B. Noheda, *Nat. Mater.* **2011**, *10*, 963.
- [34] Note that we chose a Ti composition of 60% rather than 80% because this effective Hamiltonian was technically built for concentrations close to 50%. As such both $\text{PbZr}_{0.4}\text{Ti}_{0.6}\text{O}_3$ and $\text{PbZr}_{0.2}\text{Ti}_{0.8}\text{O}_3$ have the same tetragonal P4mm ground state in their bulk forms.
- [35] G. Liu, Q. Zhang, H. H. Huang, P. Munroe, V. Nagarajan, H. Simons, Z. Hong, L.-Q. Chen, *Adv. Mater. Interfaces* **2016**, *3*, 1600444.
- [36] Due to the sensitive nature of PFM local measurement (in respect of local regions selection, probes and environment, i.e., temperature, humidity, noise level, etc.), the loops presented in Figure 5 were obtained within one hour using one same probe at several typical local points, respectively.
- [37] R. Guo, L. E. Cross, S. E. Park, B. Noheda, D. E. Cox, G. Shirane, *Phys. Rev. Lett.* **2000**, *84*, 5423.
- [38] R. J. Zeches, M. D. Rossell, J. X. Zhang, A. J. Hatt, Q. He, C. H. Yang, A. Kumar, C. H. Wang, A. Melville, C. Adamo, G. Sheng, Y. H. Chu, J. F. Ihlefeld, R. Erni, C. Ederer, V. Gopalan, L. Q. Chen, D. G. Schlom, N. A. Spaldin, L. W. Martin, R. Ramesh, *Science* **2009**, *326*, 977.
- [39] D. Atkinson, D. A. Allwood, G. Xiong, M. D. Cooke, C. C. Faulkner, R. P. Cowburn, *Nat. Mater.* **2003**, *2*, 85.
- [40] S. S. P. Parkin, M. Hayashi, L. Thomas, *Science* **2008**, *320*, 190.
- [41] G. Yu, P. Upadhyaya, Q. Shao, H. Wu, G. Yin, X. Li, C. He, W. Jiang, X. Han, P. K. Amiri, K. L. Wang, *Nano Lett.* **2017**, *17*, 261.
- [42] Y. Nahas, S. Prokhorenko, I. Kornev, L. Bellaiche, *Phys. Rev. Lett.* **2016**, *116*, 127601.
- [43] a) J. Seidel, L. W. Martin, Q. He, Q. Zhan, Y. H. Chu, A. Rother, M. E. Hawkrige, P. Maksymovych, P. Yu, M. Gajek, N. Balke, S. V. Kalinin, S. Gemming, F. Wang, G. Catalan, J. F. Scott, N. A. Spaldin, J. Orenstein, R. Ramesh, *Nat. Mater.* **2009**, *8*, 229; b) R. K. Vasudevan, A. N. Morozovska, E. A. Eliseev, J. Britson, J. C. Yang, Y. H. Chu, P. Maksymovych, L. Q. Chen, V. Nagarajan, S. V. Kalinin, *Nano Lett.* **2012**, *12*, 5524.
- [44] a) M. Gajek, M. Bibes, S. Fusil, K. Bouzehouane, J. Fontcuberta, A. E. Barthelemy, A. Fert, *Nat. Mater.* **2007**, *6*, 296; b) D. Pantel, S. Goetze, D. Hesse, M. Alexe, *Nat. Mater.* **2012**, *11*, 289; c) A. Chanthbouala, A. Crassous, V. Garcia, K. Bouzehouane, S. Fusil, X. Moya, J. Allibe, B. Dlubak, J. Grollier, S. Xavier, C. Deranlot, A. Moshar, R. Proksch, N. D. Mathur, M. Bibes, A. Barthelemy, *Nat. Nanotechnol.* **2012**, *7*, 101.
- [45] Software courtesy of Dr. Celine Lichtensteiger from the University of Geneva. Full details can be found in ref. [26b].
- [46] L. Bellaiche, A. Garcia, D. Vanderbilt, *Phys. Rev. Lett.* **2000**, *84*, 5427.